Received: 6 November 2020 | Revised: 2 April 2021 | Accepted: 14 April 2021

DOI: 10.1002/cyto.a.24356

ORIGINAL ARTICLE

MIFlowCyt

ISAC CYTOMETRY Journal of Quantitative Cell Science PART A

Detecting cells rotations for increasing the robustness of cell sizing by impedance measurements, with or without machine learning

Pierre Taraconat[1,2] | Jean-Philippe Gineys[1] | Damien Isèbe[1] | Franck Nicoud[2] | Simon Mendez[2]

[1]Horiba Medical, Parc Euromédecine, Montpellier, France

[2]Institut Montpelliérain Alexander, Grothendieck, CNRS, Univ. Montpellier, Montpellier, France

Correspondence
Simon Mendez, Institut Montpelliérain Alexander Grothendieck, CNRS, University Montpellier, France.
Email: simon.mendez@umontpellier.fr

Abstract

The Coulter principle is a widespread technique for sizing red blood cells (RBCs) in hematological analyzers. It is based on the monitoring of the electrical perturbations generated by cells passing through a micro-orifice, in which a concentrated electrical field is imposed by two electrodes. However, artifacts associated with near-wall passages in the sensing region are known to skew the statistics for RBCs sizing. This study presents numerical results that emphasize the link between the cell flow-induced rotation in the detection area and the error in its measured volume. Based on these observations, two methods are developed to identify and reject pulses impaired by cell rotation. In the first strategy, the filtering is allowed by a metric computed directly from the waveform. In the second, a numerical database is employed to train a neural network capable of detecting if the cell has experienced a rotation, given its electrical pulse. Detecting and rejecting rotation-associated pulses are shown to provide results comparable to hydrodynamical focusing, which enforces cells to flow in the center of the orifice, the gold standard implementation of the Coulter principle.

KEYWORDS

computational fluid dynamics, Coulter principle, hydrodynamic focusing, neural network, pulse editing, red blood cells

1 | INTRODUCTION

Complete blood count, which notably consists in counting and sizing blood cells, is widely employed to assess the patients' health condition. Such an analysis is performed by industrial hematological automata, that generally implement the Coulter principle [1]. As sketched in Figure 1, cells in suspension in an electrolytic solution are aspirated through a micro-orifice (aperture) in which electrodes maintain a concentrated electrical field. A cell passing through the aperture is detected by an increase of voltage at the electrodes. In addition, the maximum of this electrical pulse is assumed to be proportional to the cell volume. Screening pulses thus yields the count and the volume distribution of the analyzed cells.

Regarding red blood cells (RBCs), the mean corpuscular volume (MCV) and the RBCs distribution width (RDW) are hematological parameters of first importance for clinical decision making. In particular, the combination of MCV and RDW was historically used for classifications of anemias [2], but RDW has more recently aroused the interest of many research groups as a marker of various human disorders [3].

According to theory [4], the resistive perturbation (ΔR) produced by the cell in the detection area is related to its volume V_p as follows, assuming a perfectly insulating particle:

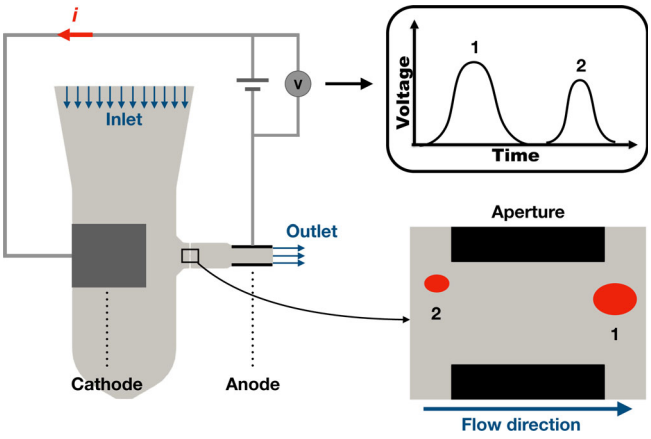

FIGURE 1 Diagram of the Coulter principle for particles counting and sizing

$$\Delta R \propto E^2 f_s V_p, \quad (1)$$

E is the electrical field and f_s the particle shape factor. Note that the voltage pulses are proportional to ΔR, as the current intensity remains constant. The shape factor characterizes how easy it is for the electrical current to go around the insulating particle, given its volume. It depends on the particle shape and orientation. For the case of deformable cells such as RBCs, f_s depends on the dynamics and deformations of the cell in the detection area. Pathologies altering the RBCs deformability and/or resting shape may thus lead to misleading diagnosis [5,6]. For instance, RBCs with abnormally high hemoglobin contents in their cytoplasm have their volume overestimated [5]. Furthermore, artifacts inherent to the implementation of the Coulter principle alter the measurements and lead to right-skewed RBC volume distributions [7,8] instead of the expected symmetrical distribution [9,10], even for normal blood samples. Indeed, measuring cells volume in a sample requires that all cells experience the same electrical field and behave identically within the aperture (in other words that all cells are associated with the same E and f_s, see Equation (1)). However, as reported in former studies, E is highly heterogeneous next to the aperture walls [4,11,12], and RBCs may rotate and deform as they flow across high-shear regions in the wall vicinity [11,13,14].

In flow cytometry, errors associated with the random orientation of asymmetrical cells with respect to the flow direction have long been understood. For instance, light scattering measurements depend on the orientation of the cell with respect to the incident laser beam and to the position of the detectors [35]. Hardware modifications may be made so that asymmetrical cells always present the same orientation to the observation device [36]. For impedance measurements, the random orientation of cells with respect to the flow direction does not generate any error: It is the flow-induced rotation of cell that changes the shape factor [11,13,14].

For impedance measurements, hydrodynamical focusing [15] overcomes measurement inaccuracies caused by cells flowing next to the walls, so that symmetrical and Gaussian-like distributions are retrieved. The principle is to pinch the sample flow with a secondary sheath flow, thus enforcing particles to follow centered trajectories. This enables standardization of f_s and E for a robust measurement, but implies a more intricate implementation of the Coulter principle [16]. Another strategy consists in removing the distorted pulses associated with cells passing near of the aperture edges from the analysis (also called pulse-editing). We provide here some examples of the numerous techniques introduced over the years. Remarking that centered paths generate 'bell-shaped' and symmetrical signatures, Dunstan et al [17] proposed to assess the pulse symmetry for rejecting spurious signals. Another method was to exclude long pulses [8]: Near the walls, flow speed is lower than at the center of the orifice; thus, RBCs impacted by near-wall effects are expected to produce longer electrical prints. However, the pulse duration depending on the particle volume, there is a relationship between the duration and the maximum of the pulse, which is disregarded with a simple threshold on the pulse duration. This explains the introduction of new pulse editing strategies taking into account both the pulse maximum and the pulse duration [18,19]. Methods combining several widths and/or several amplitudes calculated from pulses are currently implemented in commercial instruments, as suggested by the patent from Zhang et al [20]. Note that pulse editing is a more general strategy, which has for instance been used to measure the orientation of asymmetrical cells [35] or identify doublets in optical flow cytometers [21].

Easier to implement and cheaper, classical systems combined with pulse editing continue to be used, in spite of the higher robustness of hydrodynamical focusing. Among current instruments, different pulse editing methods are used, but they are not necessarily well documented. While the MCV is usually a robust measurement, RDW has been recently shown to depend on the analyzer [22]. To avoid such discrepancies, it is essential to control volume errors and properly establish the quality of pulse editing methods. In particular, while hydrodynamical focusing can be considered as the Reference [23], it is rarely used to assess the accuracy of pulse editing algorithms.

Industrial instruments generally suffer from accessibility issues, which limits the characterization of measurement artifacts and thus the design of pulse editing procedures. Recently, numerical simulation has been found to reproduce the electrical signatures observed in industrial instruments. Building upon this proof of concept (described in the Material and Methods, Section 2), the present work presents a series of simulations of electrical signatures for different trajectories of RBCs inside the sensing region of a Yumizen™ H2500 (HORIBA Medical, Montpellier, France), which is based on the Coulter principle. Results highlight the link between measurement errors and the flow-induced rotations of the cells which yields a secondary peak on the pulses (see Section 3.1). This observation is the foundation for two new pulse editing methods [24], one based on the use of a neural network (NN) and the other on a metric explicitly calculated on the pulses, designed to reject pulses associated with RBCs that rotate in the sensing region (see Section 2). When applied to experimental data (Section 3.2), both methods yield symmetrical volume distributions in agreement with results obtained with hydrodynamical focusing.

2 | MATERIALS AND METHODS

2.1 | Numerical simulations

2.1.1 | Numerical pipeline

Computing the dynamics of an RBC in the detection area is extremely challenging due to the separation of scales: RBCs are first stretched for tens of milliseconds, then pass through the sensing zone in a few microseconds [12]. To overcome this difficulty, an innovative numerical pipeline has been designed [14] to predict the dynamics of RBCs in the sensing zone and the corresponding electrical pulse, using the in-house solver YALES2BIO (https://imag.umontpellier.fr/~yales2bio/). The RBC dynamics are predicted by solving a fluid–structure interaction problem [25,26,27] between the fluid outside the RBC, the cytoplasm, and the RBC membrane. Then, from a resulting sequence of RBC states along time inside the orifice, as many electrostatic computations are performed. In each of them, one RBC position/shape is used, the cell being assumed insulating. The electrical field around the insulating cell is computed, and the additional resistance due to the presence of the cell (ΔR) is obtained by comparison with a calculation without RBC. Hence, calculating ΔR for the sequence of RBC consecutive positions leads to the resistive pulse over time, associated with the RBC path and deformation in the aperture. This numerical setup has been detailed and validated previously [14]. More details on the numerical setup can be found in the Supplementary Materials.

2.1.2 | Simulated cases

In this work, the role of numerical simulations is twofold: Understanding measurement inconsistencies induced by cells flowing near the aperture edges; building a numerical database for the training of a NN capable of rejecting pulses irrelevant to volume assessments.

With the aim of investigating the impact of RBC paths on the impedance measurements, several trajectories are simulated while maintaining cell parameters constant. The RBC is represented as a discoid of volume 93 μm^3, whose shape has been defined analytically [28]. The RBC has an aspect ratio $\mathcal{Q}$ of 0.65, with $\mathcal{Q}$ defined as the ratio between the cell volume and the volume of the sphere having the same surface area as the RBC. The mechanical model of the RBC membrane reproduces its composite structure, with different submodels representing the lipid bilayer of the membrane and its cytoskeleton [29,30]. This modeling is now classical and has been successfully applied and validated in numerous situations [14,25,26,27]. The membrane mechanics is notably parameterized by the shear modulus G_s, the area modulus E_a, the bending modulus E_b. In agreement with measurements available in the literature [31,32], we set: $G_s = 2.5 \times 10^{-6}$ N m^{-1}; $E_a = 2.5 \times 10^{-1}$ N m^{-1}; $E_b = 6.0 \times 10^{-19}$ N m. The viscosity of the suspending medium is $\nu_{\text{ext}} = 10^{-6}$ m^2 s^{-1} and its conductivity $\sigma_{\text{ext}} = 2.27$ S m^{-1}. Regarding the fluid inside the RBC membrane, a viscosity ν_{in} of 18.0×10^{-6} m^2 s^{-1} is set, which is representative of viscosity values of hemoglobin solutions at ambient temperature [32]. Ten different trajectories are investigated, from the axis of the orifice to the near-wall region.

A numerical database is built for training a NN capable of detecting if an RBC rotates in the aperture, given the associated electrical pulse. In order to make the NN robust with respect to cells rheology and morphology, RBC parameters were varied in the following ranges to build the database: $\nu_{\text{in}} \in (15.0 \times 10^{-6}, 20.0 \times 10^{-6}$ m^2 s$^{-1})$; $G_s \in (2.5 \times 10^{-6}, 160.0 \times 10^{-6}$ N m$^{-1})$; $V_p \in (85, 100\ \mu$m$^3)$; $\mathcal{Q} \in (0.65, 0.85)$. Altogether, the database is composed of 78 cases. All simulations are performed by considering the industrial geometry and operating regime provided by HORIBA Medical and illustrated in Figure 1, which characterize the Yumizen™ H2500 (HORIBA medical, Montpellier, France). More precisely, the aperture has a diameter of 50 μm, a length of 75 μm and the pressure drop ensuring the flow is of 200 mbar.

2.2 | Detection of the particle flow-induced rotation

As reported in the literature [10,11], complex pulses shapes are obtained when deformable and aspherical particles flow near the aperture wall, while 'bell-shaped' signatures are obtained for centered paths. Previously [14], we directly showed that RBCs deform and, most importantly, rotate when flowing near the wall, which induces a peak on the electrical pulse at the exact moment of the flow-induced rotation. Golibersuch [13] also reported pulses presenting several peaks when the aperture is long enough to allow RBCs to rotate several times in the sensing region. Our pulse editing procedures consist in detecting such rotations on the electrical pulses, in order to only conserve 'bell-shaped' signatures from centered trajectories.

In the first method, 'bell-shaped' signatures are isolated by thresholding a metric directly calculated from the pulses. With $\mathcal{H}$ the maximum of the pulse, whatever the quantity analyzed (voltage or resistance), let us define $\mathcal{W}_u$ and $\mathcal{W}_d$, two pulse widths computed with thresholds $\mathcal{H} \times p_u$ and $\mathcal{H} \times p_d$, respectively, (see Figure 2). p_u and p_d are included in (0,1), with $p_u > p_d$. We introduce $\mathcal{R}$, the ratio between $\mathcal{W}_u$ and $\mathcal{W}_d$:

$$\mathcal{R} = \frac{\mathcal{W}_u}{\mathcal{W}_d} \times 100. \tag{2}$$

the parameter p_d is chosen in such a way that $\mathcal{H} \times p_d$ intersects the ascending and descending slopes of the pulse, and $\mathcal{W}_d$ informs on the time spent by the particle in the micro-orifice. If a secondary peak is present on the pulse, $\mathcal{W}_u$ is meant to measure its duration. Hence, p_u must be defined so that $\mathcal{H} \times p_u$ crosses the peak. Note that in the absence of peak, $\mathcal{W}_u$ should be closer to $\mathcal{W}_d$. Hence, $\mathcal{R}$ is expected to be small in the case of a flow-induced rotation peak (see Figure 2(B)) and larger for a 'bell-shaped' pulse without peak (see Figure 2(C)). The filtering then consists in applying a rejection threshold on the metric $\mathcal{R}$. In practice, we have used $p_u = 7/8$ and $p_d = 1/2$. However, tests

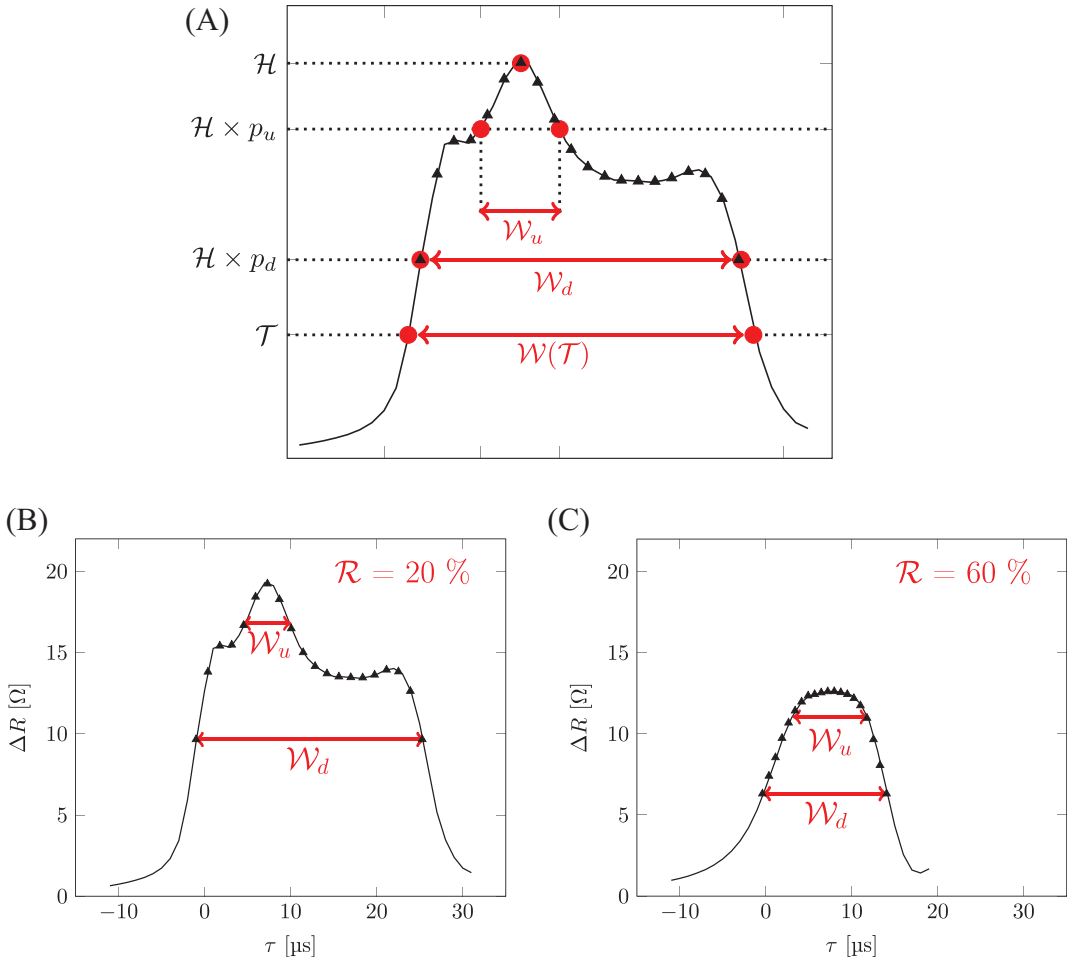

FIGURE 2 (A) Illustration of quantities computed from an electrical pulse. In particular, $\mathcal{W}_u$ and $\mathcal{W}_d$ required for assessing the $\mathcal{R}$ metric are depicted. Let us define in general $\mathcal{W}(\mathcal{T})$ as the pulse width calculated with a threshold $\mathcal{T}$. Then, we define $\mathcal{W}_u = \mathcal{W}(\mathcal{H} \times p_u)$ and $\mathcal{W}_d = \mathcal{W}(\mathcal{H} \times p_d)$, with $\mathcal{H}$ the pulse maximum. Calculations of $\mathcal{R}$ for a complex signature presenting a peak and a 'bell-shaped' pulse are given in (B) and (C), respectively. Black triangles depicted in the graphs illustrate the resampling performed on the waveforms in order to make them intelligible by the neural network (NN). This is required to represent all pulses with the same number of variables

shown as Supplementary Materials support that the quality of the results does not depend on the exact values of these thresholds.

In the second method, the filtering is performed by a NN. A simple multi-layer perceptron of three layers is sufficient to address this clustering problem. The first layer is composed of 21 neurons and takes the pulse as an input. Pulses are resampled into 20 values by taking into account the part of the curve located above $\mathcal{H} \times p_d$, as illustrated by black triangles in Figure 2(A). These 20 values are normalized by $\mathcal{H}$ and given as inputs to the NN, in addition to $\mathcal{W}_d$. This way, pulses of different durations are all expressed with the same number of variables (see Figure 2(B), (C)). The reworked pulse is propagated into the NN through the single hidden layer of 20 neurons toward the output layer, composed of a sole neuron. Sigmoid activation functions are associated to all neurons of the model. Hence, the NN renders a score included between 0 and 1. A database of 78 numerical pulses is considered for the model training. Pulses are associated to target values of 0 or 1 whether the RBC has turned in the aperture or not. Then, numerical pulses are split into a training dataset made of 62 observations and a test dataset of 16 pulses. The learning step is done on the training dataset in 10,000 epochs with a batch size of 62 (the size of the training dataset) with the ADAM algorithm (a variant of the gradient descent method) which aims at minimizing the RMS error between NN predictions and target values. When applied to the test dataset, the NN is found to properly isolate pulses associated to rotating RBCs from others by applying a threshold of 0.5 on NN scores. More information about the database and the preliminary tests is provided as Supplementary Materials. The NN implementation is done by means of the python library TensorFlow™ [33] (GOOGLE Inc.) which is publicly available (https://www.tensorflow.org).

2.3 | Experimental tests

2.3.1 | Experiment overview

To assess the accuracy of the pulse-editing methods, results from an analyzer with the classical implementation of the Coulter principle

combined with pulse editing are compared for each blood sample with measurements from a device using hydrodynamical focusing. Distribution of measured volumes, MCV, and RDW are considered for the comparisons.

2.3.2 | Flow sample and specimen description

Human peripheral blood samples were collected from 20 healthy donors in K3EDTA tubes (VACUETTE™) and analyzed within the 6 h after withdrawal. They were obtained from Etablissement Français du Sang, Montpellier, France.

2.3.3 | Instrument

The analyses are performed with a Yumizen™ H2500 commercialized by HORIBA Medical. In the present work, two units of the Yumizen H2500 are considered: the device dedicated to the RBCs analysis based on the Coulter principle, and the system normally dedicated to the optical platelet detection, in which hydrodynamical focusing is used. In the first one, RBCs are counted and sized by the use of a classical implementation of the Coulter principle (as in Figure 1). Here, the second unit is not used for its original purpose, but to count and size RBCs with hydrodynamical focusing, to provide reference results. For each blood sample, electrical pulses coming from the two units are recorded separately. This is done by a dedicated in-house LabVIEW™ (National Instruments) code, detailed in the Supplementary Materials. Acquisitions from the unit classically dedicated to RBCs are labeled noHF, while the acquisitions from the hydrofocused platelet detector used here for sizing RBCs are referred to as HF. Numerical simulations are relevant to the classical implementation of the Coulter principle, thus to measurements labeled by noHF.

3 | RESULTS

3.1 | Detection of the particle flow-induced rotation from the associated pulse

This section introduces the fundamental concept from which the filters of Section 2.2 are designed. More precisely, the impact of the flow-induced cell rotation on the measured volume and its relationship with the trajectory are explained, keeping the intrinsic properties of the RBC strictly identical. Considering the 10 possible RBC trajectories depicted in Figure 3(A), electrical signatures are computed (Figure 3(B)). The non-dimensional resistive perturbations ΔR^* are obtained by scaling ΔR by the pulse maximum (viz. $\mathcal{H}$) of the centered path (Case 1), which is supposed to be a correct measure for the RBC volume, free of edge effects. As the same RBC is considered for all cases, $\mathcal{H}^*$, the maximum of ΔR^* pulses, informs about the errors in the volume measurement associated with the RBC trajectory. In an 'ideal' system, $\mathcal{H}^* = 1.0$ independently of the trajectory.

The closer to the orifice edges is the particle path, the longer the pulse duration, which makes it easy to order the pulses. For the most centered paths (Cases 1–4), the pulses are 'bell-shaped' while more complex signatures are observed for the near-wall trajectories (Cases 5–10). Figure 3(C), (D) show RBC consecutive positions in the orifice for Cases 1 and 10, respectively. The RBC flowing along the axis (Figure 3(C)) displays an elongated shape aligned with the orifice axis. In contrast, an RBC evolving near the aperture edges rotates, which induces a peak on the electrical perturbation, as highlighted by the black arrows in Figure 3(D), (E). In industrial instruments, high-speed flows are used to ensure a high throughput. Hence, high shear stresses result in rotation and deformation of the RBCs, which cause an increase of shape factor f_s and a peak on the electrical pulse. The time of exposure to the shear and the shear level depend on the trajectory, which explains the variety of electrical signatures (Cases 5–10, Figure 3(B)).

In the Coulter principle, the pulse maximum is supposed to be proportional to the particle volume. Figure 3(B) thus shows that the apparent volume of an RBC depends on the RBC trajectory. For instance, comparing the maxima of Cases 1 and 10 in Figure 3(B) demonstrates that an RBC flowing near the wall is seen 1.53 times bigger than if it had flowed near the aperture axis. Figure 4(A) displays the different non-dimensional measured volumes $\mathcal{H}^*$ as a function of the cell distance to the aperture axis (D), for different internal viscosities ν_{in}. Regarding case $\nu_{\text{in}} = 18.0 \times 10^{-6}\ \text{m}^2\,\text{s}^{-1}$ in Figure 4(A), $\mathcal{H}^*$ is close to 1.0 in the core region of the aperture ($D \in [0; 13\ \mu m]$). With the perfectly centered path as the reference, the error at $D = 13\ \mu m$ is about 3%. $\mathcal{H}^*$ increases with D between 13 and 17 μm, then stabilizes around a value of 1.53. These volume overestimates for near-wall trajectories (D >13 μm) explain the typical 'right-skewed' volume distributions observed experimentally [7,8]. Simulations also show that for near-wall trajectories, the apparent volume increases with the internal viscosity (see Figure 4(A)). This confirms the experiments of Mohandas et al [5] which showed an overestimation of the MCV when the hemoglobin content of RBCs is abnormally high (which corresponds to high cytoplasm viscosity). Consequently, removing near-wall trajectories has two advantages: Avoiding sizing errors in general and making measurements robust to variations in the hemoglobin content of the RBCs.

As defined in Figure 4(B), the orientation of the cell when the pulse maximum is reached, θ_m, is computed and displayed in Figure 4 (C). If D >16 μm, the time spent by the cell in the detection area is sufficiently long and the shear undergone by the particle large enough for the RBC to reach a 90° orientation inside of the aperture: The RBC is then perpendicular to the electrical field. On the contrary, in the core region of the micro-orifice, the cell barely rotates and $\theta_m \approx 0^\circ$ when D <13 μm. Between 13 and 16 μm, the cell starts rotating, but does not spend enough time in the aperture to reach $\theta_m = 90^\circ$. The fact that both $\mathcal{H}^*$ and θ_m display a similar sigmoid-like profile (see Figure 4(A), (C)) supports the approach of detecting the flow-induced RBC rotation for pulse edition to improve the volume assessment.

The evolution of the metric $\mathcal{R}$ (see Equation (2)) with D is shown in Figure 4(D). When θ_m is small (D <13 μm), high values of $\mathcal{R}$ are

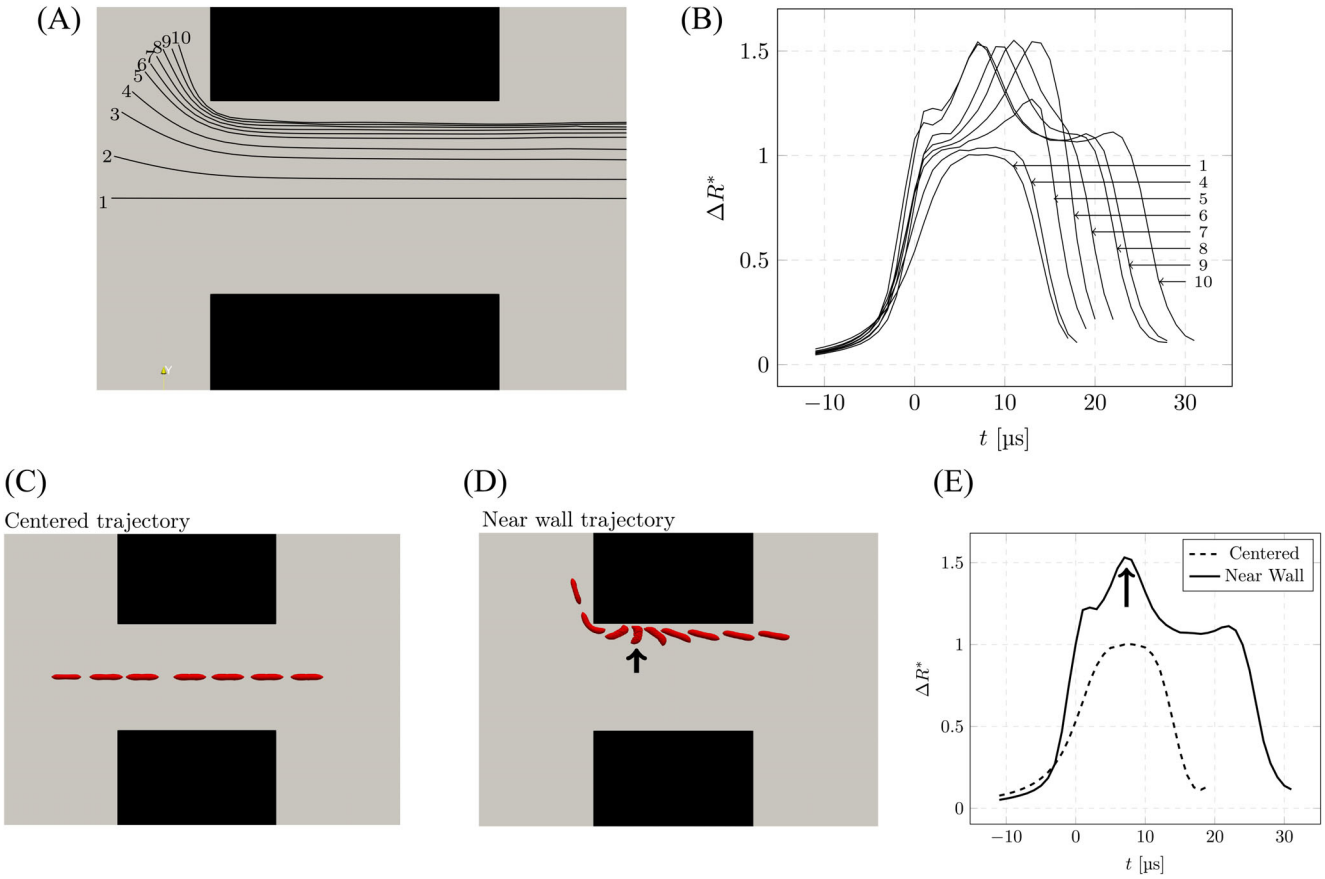

FIGURE 3 Simulated impedance pulses for different virtual trajectories of a red blood cell (RBC) in the sensing region. All results in this figure were obtained with the same RBC characteristics: $\nu_{in} = 18.0 \times 10^{-6}$ m^2 s^{-1}, $G_s = 2.5 \times 10^{-6}$ N m^{-1}, $E_a = 2.5 \times 10^{-1}$ N m^{-1}, $E_b = 6.0 \times 10^{-19}$ J, $V_p = 93\ \mu m^3$, and $\mathcal{Q} = 0.65$. The considered trajectories are shown in (A) and the corresponding pulses in (B). The pulses amplitudes in (B) are scaled with the maximum of Case 1 (the centered path) which equals 12.6 Ω. For sake of clarity, Cases 2 and 3 are not shown in (B). Pictures (C) and (D) show a series of RBC consecutive positions inside the aperture for Cases 1 and 10, respectively. Figure (E) recall the electrical signatures related to RBC dynamics of (C) and (D). The cell rotation (D) generates a peak on the associated impedance pulse, as highlighted by black arrows in (D) and (E)

obtained (between 60% and 70%), while for cases where the RBCs may reach $\theta_m = 90^\circ$ (D >16 μm), $\mathcal{R}$ is below 30%. By comparing Figure 4(A), (D), it is seen that rejecting pulses for which $\mathcal{R}$ is below 55% would for instance allow reducing the volume overestimation ($\mathcal{H}$) from 53% to 10%. Thus, a pulse editing method with a threshold on $\mathcal{R}$ is expected to separate pulses from rotating RBCs and 'bell-shaped' pulses, for which RBCs do not rotate. For the NN-based pulse editing method, each numerical pulse is associated with a target NN score of 1 or 0, whether θ_m is lower or higher than 15°, respectively.

Our pulse editing algorithms have been designed using simulated data. As a consequence, their success depends on how accurate and representative the numerical results are with respect to real data. In a previous study, we have proven that simulation is able to predict relevant pulses both for RBCs and rigid spherical beads [14]. Further comparisons for RBCs are presented in the Supplementary Materials to show the excellent agreement between pulse shapes. Overall, all simulated pulse shapes are found in the experiments, and they are representative of the vast majority of the actual pulses (about 92%). However, experiments may feature other pulses, corresponding for instance to doublets or other blood cells, that can be easily separated from the RBC pulses.

Pulse editing methods based on the detection of the flow-induced RBC rotation are next tested on experimental data to quantify the improvement in the accuracy of the hematological parameters related to the RBCs volumes, the MCV, and the RDW.

3.2 | Application to experimental data

Let us consider two acquisitions performed on the same blood sample, but obtained with the classical (noHF) and the hydrofocused systems (HF). For each pulse coming from the classical acquisition, the maximum $\mathcal{H}$ of the voltage perturbation, the width ratio $\mathcal{R}$ and the NN score are computed. Figure 5 shows the scatter plot of $\mathcal{R}$ as a function of $\mathcal{H}$ by coloring the data points according the NN scores, for the acquisition noHF. Two distinct clusters separated by a threshold of $\mathcal{R} = 52\%$ are observed in Figure 5. This threshold is close to the value of 55% that was predicted numerically. Note that for the cluster

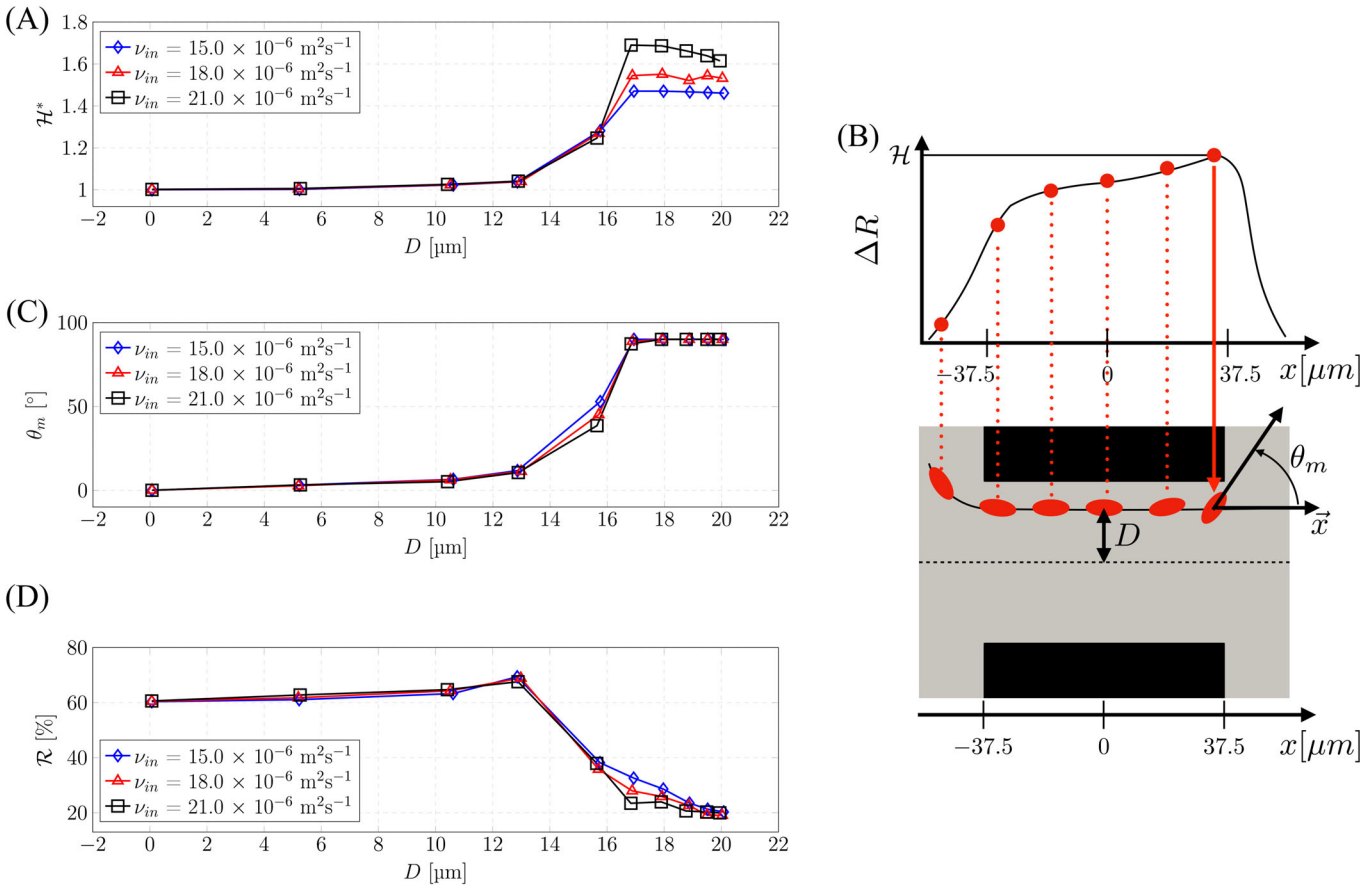

FIGURE 4 Evolution of the measured apparent volume, presented here with the non-dimensional form $\mathcal{H}^*$(A), the particle orientation θ_m when the pulse reaches its maximum value (C), and the metric $\mathcal{R}$ (D), with the distance from orifice centerline D. Picture (B) illustrates how the distance from the aperture center D and the orientation θ_m are defined. In (A), (C), and (D), results are shown for different internal viscosities ν_{in}, the remaining RBCs parameters being set to: $G_s = 2.5 \times 10^{-6}$ N m^{-1}; $E_a = 2.5 \times 10^{-1}$ N m^{-1}; $E_b = 6.0 \times 10^{-19}$ J; $V_p = 93$ µm^3; $\mathcal{Q} = 0.65$

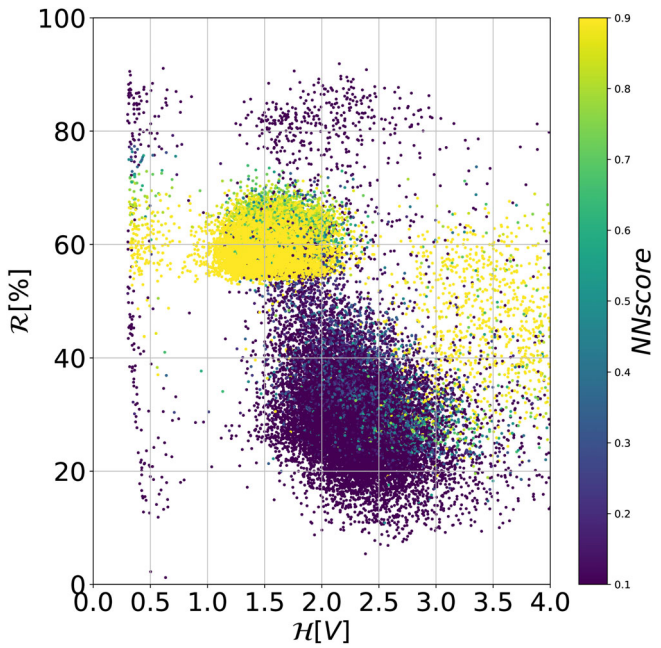

FIGURE 5 Scatter plot of the width ratios ($\mathcal{R}$) according to the pulses maximums ($\mathcal{H}$) by coloring points according to the neural network (NN) predictions (NN score)

located below $\mathcal{R}$ = 52%, $\mathcal{H}$ is between 1.6 and 3.0 V, while for the cluster above $\mathcal{R}$ = 52%, $\mathcal{H}$ is between 1.0 and 2.25 V. This is consistent with the numerical results, which show that pulses with low $\mathcal{R}$ are associated with cell rotation and volume overestimation (see Figure 4(A), (C), and (D)). The NN modeling provides a clustering globally equivalent to $\mathcal{R}$. Indeed, for $\mathcal{R}$ above 52%, NN scores are close to 1, while below 52%, values close to 0 are predicted by the NN.

Minor populations are also visible in Figure 5. First, measurements at $\mathcal{H}$ below 0.75 V are associated with platelets. Then, the widespread population around $\mathcal{H}$ = 3.5 V results from doublets or bubbles in the aperture. Finally, measurements at $\mathcal{R} \approx 80\%$ may be explained by pulses presenting a small peak so that $\mathcal{W}_u$ does not measure the time spent in the peak. This could be induced by doublets or quasi-spherical RBCs, such as echinocytes. Note that the parameter p_u may be increased in order to handle pulses with a small peak as well. Otherwise, such minor populations could be discarded by applying relevant thresholds on $\mathcal{R}$ or $\mathcal{H}$.

In the following, we investigate the effect of rejecting pulses associated with rotating RBCs from the statistical analysis. Two removal methods are assessed: $\mathcal{R}$ <52% and NN score <0.5. By doing so, roughly 46% of the pulses are discarded. The distributions of $\mathcal{H}$ obtained with the classical counter and the hydrofocused counter are

shown in Figure 6(A). Note that the signals are treated and amplified differently in the two counters, which explains the offset between the distributions, and that the number of RBCs measured is different. Nonetheless, a first observation is that hydrodynamical focusing yields a symmetrical and Gaussian-like distribution while a right-skewed volume distribution is obtained with the classical system. However, rejecting pulses with $\mathcal{R}$ below 52% or with NN scores below 0.5 is shown to render symmetrical distributions (cases noHF- $\mathcal{R}$ and noHF-NN in Figure 6(A)).

In order to provide a quantitative comparison between both systems, measurements are calibrated before computing the probability density functions of cells volumes depicted in Figure 6(B). Voltage pulses are calibrated in such a way that the averaged $\mathcal{H}$ for cases HF and noHF- $\mathcal{R}$ (see Figure 6(A)) correspond to the MCV rendered by a ABX Pentra™ DX120 (HORIBA Medical), used as a reference machine. As shown by Figure 6(B), a good comparison is observed between hydrofocused and classical systems, provided that a rotation filter is used (see noHF- $\mathcal{R}$ and noHF-NN in Figure 6(B)).

Electrical pulses from the classical and the hydrofocused devices were recorded for 20 blood samples in total. After calibration, mean cells volumes (MCV) and RDWs were calculated. The MCV is the mean of V_p and the RDW is computed as the standard deviation of V_p, divided by the MCV. MCV and RDW are calculated from the amplitudes distribution, by discarding the part of the curve that falls below 5% of the maximum occurrence, which naturally excludes platelets and doublets associated with large volumes. The distribution curve is smoothed with a moving average algorithm prior the calculation of MCV and RDW. Correlations of MCV and RDW between the hydrofocused system and the classical system with different filters are shown in Figure 6(C), (D), respectively. Regarding the MCV (Figure 6 (C)), good Pearson correlation coefficients (R) are obtained for all cases, even without sorting the pulses: When pulses are not sorted, the MCV is consistently overestimated by 20%–25% in our setup. Considering the RDW, results show that unfiltered data from the classical system are poorly correlated with hydrodynamical focusing (see case noHF in Figure 6(D), $R = 0.75$). The correlation is significantly

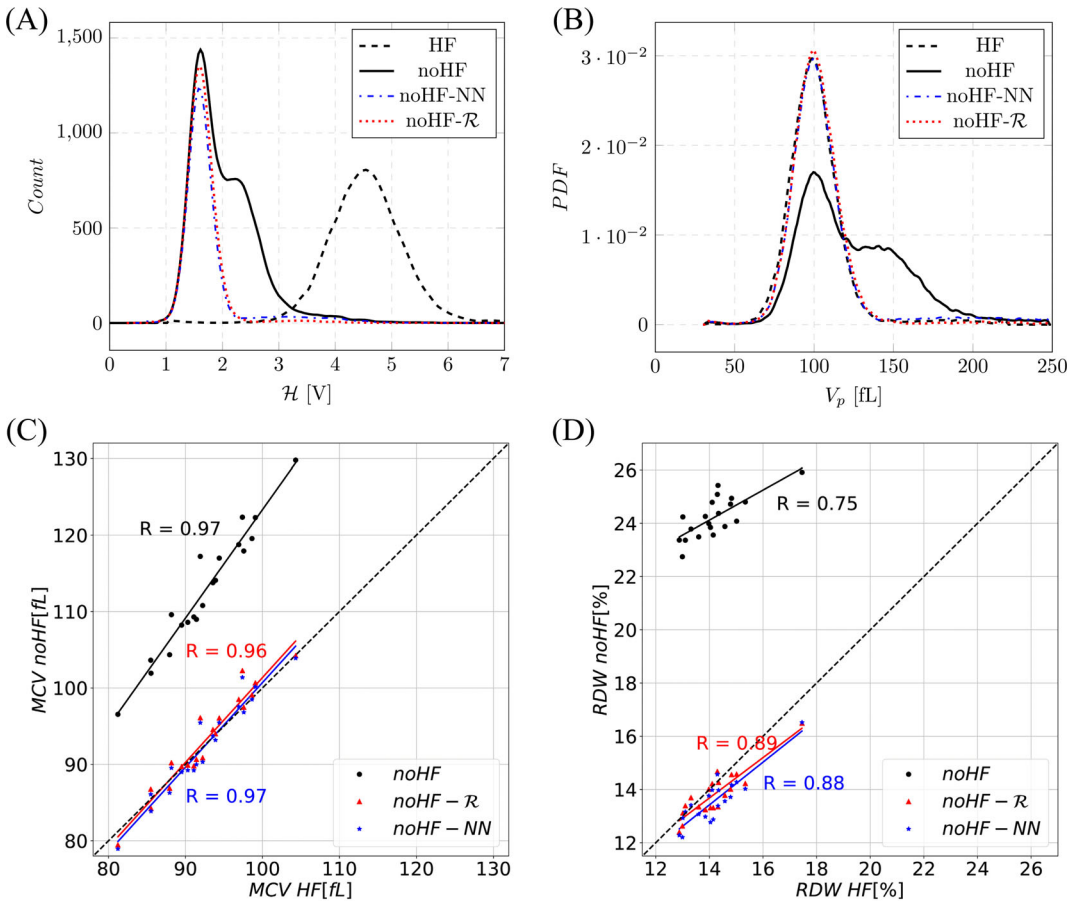

FIGURE 6 (A) Histograms of pulses maxima obtained from the classical system (noHF) and the system with hydrodynamic focusing (HF) when analyzing a blood sample from a healthy donor. Case noHF- $\mathcal{R}$ is obtained by applying $\mathcal{R}$ <52% as a rejection criterion, while noHF-neural network (NN) results from the removal of pulses whose NN score is below 0.5. (B) Probability density functions of red blood cellS (RBCs) volumes, derived from pulses heights $\mathcal{H}$, after calibration. Correlations of mean cell volumes (C) and RBCs distribution widths (D), between the classical system and the hydrofocused analyzer, with and without filters

improved to 0.88 and 0.89 with the use of the $\mathcal{R}$ based filter and the NN modeling, respectively.

4 | DISCUSSION

For counting and sizing RBCs, impedance-based systems using the Coulter principle without hydrodynamical focusing remain widely used, because of their low fluid consumption, the simplicity of their implementation and their lower cost.

The present study provides new insights on inaccuracies in the sizing of RBCs in such analyzers. Using numerical simulations, we showed 'bell-shaped' pulses when cells flow in the aperture core. On the opposite, a variety of complex signatures are obtained when cells flow near the wall: There, velocity gradients make RBCs rotate, which generates a peak on the electrical pulse, leading in turn to overestimated RBCs volumes and right-skewed distributions. Furthermore, this volume overestimation is shown to depend on the RBCs rheology. Novel pulse editing methods are then proposed to reject pulses affected by near-wall effects. In the first approach, the rotation associated peak is detected by computing and thresholding a metric ($\mathcal{R}$) calculated from the pulse. In the second, 'bell-shaped' signatures of central trajectories are isolated using a NN trained from numerical simulations. These methods retrieve symmetrical RBC volume distributions, in agreement with results from a system with hydrodynamic focusing, which can be considered as the reference. Besides, very good correlations are obtained with the reference in terms of MCV and RDW with the two methods.

Further assessments of our approach are intended in the near future. Since both filters provide close results, we will focus on the $\mathcal{R}$-based one, which is easier to implement on the automata as compared with the NN. Actually, we are currently integrating the $\mathcal{R}$-based filter in the analyzer to apply it automatically and avoid time-consuming data transfer and application of the filter on the personal computer, as it was done in this proof of concept. In addition, we plan to apply this method to other blood samples with wider variations in MCV and RDW (for instance using pathological samples) to challenge the filter.

The proposed filters are meant to detect flow-induced rotations of particles. Note that in the case of more spherical particles, the problem of rotation-associated overestimation of the volume disappears. However, small electrical peaks [34,4,14] may be present at the corner of the orifice. The parameters of the $\mathcal{R}$-based filter could be modified to detect such peaks, as discussed in Section 3.2.

Some blood analyzers use surfactants to modify the RBCs and make them spherical, so that the sizing is more robust. The use of a rotation-based filter may make the use of such complex and possibly costly external fluids useless.

Filtering the data using $\mathcal{R}$, which is a ratio of pulse widths, has advantages and drawbacks: First, such a filter has two relative threshold parameters that define the widths used to calculate $\mathcal{R}$. These parameters, p_u and p_d, need to be tuned and may depend on the external fluid used, the geometry, the flow speed and the type of particles to size. In general, when adapting the $\mathcal{R}$-based filter to a new machine, preliminary tests are needed to check and adapt p_u, p_d and the threshold value of $\mathcal{R}$ to reject or accept the pulses. However, we have seen that the filter is not very sensitive to the values of those thresholds (as illustrated in the supplementary materials). In addition, the tuning process is easy, as the $\mathcal{R}$-based filter should separate the pulses into two well-defined subpopulations, as shown in Figure 5. Such a property of the $\mathcal{R}$-based filter is actually a major advantage compared to other pulse editing methods [8,17,19,20]. One reason for this is that $\mathcal{R}$ is actually independent of the RBC volume, which is not the case of many other metrics used for pulse editing, such as the pulse width [8]. This also guarantees a better robustness of the filter. In addition, note that some filters based on the symmetry of the pulse would not reject some near-wall symmetric pulses, while the $\mathcal{R}$-based filter does.

While many analyzers implement pulse editing methods, they are rarely documented in a thorough way, and a stricter quality assessment would be beneficial. In particular, we stress that it is possible to have a true validation of pulse editing methods by comparing the pulse edited data with data obtained in systems with hydrodynamic focusing for the same blood, as presented in this article, and by comparing not only the MCV but also the RDW, which is more sensitive to errors and is more and more employed as a diagnostic parameter [3].

Finally, cells orientation in flow cytometers has been reported to alter the optical measurements [35,36]. Numerical simulations of cells dynamics in such devices could bring new understanding on such artifacts and potentially assist the development of more robust flow cytometers.

AUTHOR CONTRIBUTIONS

Pierre Taraconat: Conceptualization, Methodology, Writing—Original Draft, Writing—Review & Editing, Investigation: performed the numerical simulations and the experimental acquisitions, Formal analysis. **Jean-Philippe Gineys**: Conceptualization, Methodology, Investigation: Performed the experimental acquisitions, Resources: Settiing up the experiments. **Damien Isèbe**: Conceptualization, Methodology, Supervision. **Franck Nicoud**: Conceptualization, Methodology, Supervision, Software: Supported and assisted the numerical investigations. **Simon Mendez**: Conceptualization, Methodology, Supervision, Writing—Original Draft, Writing—Review and Editing, Software: Supported and assisted the numerical investigations.

ORCID

Pierre Taraconat https://orcid.org/0000-0002-6847-0856
Franck Nicoud https://orcid.org/0000-0002-0006-8422
Simon Mendez https://orcid.org/0000-0002-0863-2024

REFERENCES

1. Coulter WH. Means for counting particles suspended in a fluid.US Patent 2,656,508. 1953.
2. Evans TC, Jehle D. The red blood cell distribution width. J Emerg Med. 1991;9:71–4. https://doi.org/10.1016/0736-4679(91)90592-4.

3. Salvagno GL, Sanchis-Gomar F, Picanza A, Lippi G. Red blood cell distribution width: a simple parameter with multiple clinical applications. Crit Rev Clin Lab Sci. 2014;52(2):86–105. https://doi.org/10.3109/10408363.2014.992064.
4. Kachel V. Sizing of cells by the electrical resistance pulse technique: methodology and application in cytometric systems. Cell Analysis. 1982;1:195–331.
5. Mohandas N, Clark MR, Kissinger S, Bayer C, Shohet SB. Inaccuracies associated with the automated measurement of mean cell hemoglobin concentration in dehydrated cells. Blood. 1981;56(1):125–128.
6. Strauchen JA, Alston W, Anderson J, Gustafson Z, Fajardo LF. Inaccuracy in automated measurement of hematocrit and corpuscular indices in the presence of severe hyperglycemia. Blood. 1981;57(6):1065–7.
7. Brian SB. On the distribution of red cell volumes. Blood. 1968;31:503–15.
8. Waterman CS, Atkinson EEJ, Wilkins BJ, Fischer CL, Kimzey SL. Improved measurement of erythrocyte volume distribution by aperture-counter signal analysis. Clin Chem. 1975;21(9):1201–11.
9. Price-Jones C. The diameters of red cells in pernicious anæmia and in anæmia following hæmorrhage. J Pathol Bacteriol. 1922;25(4):487–504. https://doi.org/10.1002/path.1700250410.
10. Grover NB, Naaman J, Ben-Sasson S, Doljanski F. Electrical sizing of particles in suspensions: III. Rigid spheroids and red blood cells. Biophys J. 1972;12(9);1099–116.
11. Kachel V. Electrical resistance pulse sizing: Coulter sizing. In: Melamed MR, Lindmo T, Mendelsohn ML, eds. Flow Cytometry and Sorting, 2nd ed. New York: Wiley-Liss, Inc.; 1990.p. 45–80.
12. Isèbe D, Nérin P. Numerical simulation of particle dynamics in an orifice-electrode system. Application to counting and sizing by impedance measurement. Int J Numer Method Biomed Eng. 2013;29(4):462–75.
13. Golibersuch D. Observation of Aspherical particle rotation in Poiseuille flow via the resistance pulse technique: I application to human erythrocytes. Biophys J. 1973;13(3):265–80.
14. Taraconat P, Gineys JP, Isebe D, Nicoud F, Mendez S. Numerical simulation of deformable particles in a Coulter counter. Int J Numer Method Biomed Eng. 2019;35:e3243. https://doi.org/10.1002/cnm.3243.
15. Spielman LGSL. Improving resolution in Coulter counting by hydrodynamic focusing. J Colloid Interface Sci. 1968;26:175–82.
16. Tatsumi N, Tsuda I, Fujimoto K, Matsumoto H. Evaluation of a new blood cell counter with sheath flow system. Cytometry. 1985;6(5):395–400.
17. Dunstan HJ, Harfield JG, Knight P, Podgorney HJ. Method and apparatus for editing particle produced electrical pulses.US Patent 4,797,624. 1989.
18. Lombarts AJPF, Koevoet AL, Leijnse B. Basic principles and problems of Haemocytometry. Ann Clin Biochem. 1986;23(4):390–404. https://doi.org/10.1177/000456328602300404.
19. Ishizuka K, Matsubayashi H, Nishimori M. Particle counting method and particle counting apparatus.WO Patent 2015099116 A1. 2015.
20. Zhang S, Zheng M, Lin D, Huo Z. Systems and methods for particle counting.US Patent 7,457,709 B2. 2008.
21. Donnenberg AD, Donnenberg VS. Rare-event analysis in flow cytometry. Clin Lab Med. 2007;27(3):627–52. https://doi.org/10.1016/j.cll.2007.05.013.
22. Lippi G, Pavesi F, Bardi M, Pipitone S. Lack of harmonization of red blood cell distribution width (RDW). Evaluation of four hematological analyzers. Clin Biochem. 2014;47(12):1100–3. https://doi.org/10.1016/j.clinbiochem.2014.06.003.
23. Behrens WV, Edmondson S. Comparison of techniques improving the resolution of standard Coulter cell sizing systems. J Histochem Cytochem. 1976;24(1):247–56. https://doi.org/10.1177/24.1.1254920.
24. Taraconat P, Isebe D, Mendez S, Nicoud F. Device for medical analyses with impedance signal processing.WO Patent 2020216952. 2020.
25. Lanotte L, Mauer J, Mendez S, Fedosov DA, Fromental JM, Claveria V, et al. Red cells' dynamic morphologies govern blood shear thinning under microcirculatory flow conditions. Proc Natl Acad Sci U S A. 2016;113(47):13289–94.
26. Sigüenza J, Mendez S, Nicoud F. How should the optical tweezers experiment be used to characterize the red blood cell membrane mechanics? Biomech Model Mechanobiol. 2017;16:1645–57.
27. Mendez S, Abkarian M. In-plane elasticity controls the full dynamics of red blood cells in shear flow. Phys Rev Fluids. 2018;3:101101.
28. Evans EA, Fung YC. Improved measurements of the erythrocyte geometry. Microvasc Res. 1972;4:335–47.
29. Skalak R, Tozeren A, Zarda RP, Chien S. Strain energy function of red blood cell membranes. Biophys J. 1973;13:245–64.
30. Helfrich W. Elastic properties of lipid bilayers: theory and possible experiments. Z Naturforsch. 1973;28 c:693–703.
31. Abkarian M, Viallat A. Fluid-structure interactions in Low-Reynolds-Number Flows. On the importance of red blood cells deformability in blood flow. London: *Royal Society of Chemistry*; 2016. p. 347–462.
32. Mendez S, Abkarian M. Single red blood cell dynamics in shear flow and their role in hemorheology. In: Dynamics of blood cell suspensions in microflows, Boca Raton FL: CRC Press; 2019:125–181.
33. Abadi M, Agarwal A, Barham P, et al. TensorFlow: a system for large-scale machine learning. Proc. 12th USENIX Conf. Operating Systems Design and Implementation. 2016:265–283.
34. Grover NB, Naaman J, Ben-Sasson S, Doljanski F. Electrical sizing of particles in suspensions: I Theory. Biophys J. 1969;9:1398–414.
35. Loken MR, Parks DR, Herzenberg LA. Identification of cell asymmetry and orientation by light scattering. J Histochem Cytochem. 1977;25(7):790–5. https://doi.org/10.1177/25.7.330730.
36. Stovel R, Sweet R, Herzenberg L. A means for orienting flat cells in flow systems. Biophys J. 1978;23(1):1–5. https://doi.org/10.1016/S00063495(78)85427-7.

SUPPORTING INFORMATION

Additional supporting information may be found online in the Supporting Information section at the end of this article.

How to cite this article: Taraconat P, Gineys J-P, Isèbe D, Nicoud F, Mendez S. Detecting cells rotations for increasing the robustness of cell sizing by impedance measurements, with or without machine learning. Cytometry. 2021;1–10. https://doi.org/10.1002/cyto.a.24356